18. Crovisier, J. *et al.* The spectrum of Comet Hale-Bopp (C/1995 01) observed with the Infrared Space Observatory at 2.9 AU from the Sun. *Science* **275**, 1904–1907 (1997).

19. Molster, F. J., Waters, L. B. F. M., Tielens, A. G. G. M., Koike, C. & Chihara, H. Crystalline silicate dust around evolved stars. III. A correlations study of crystalline silicate features. *Astron. Astrophys.* **382**, 241–255 (2002).

20. Malfait, K. *et al.* The spectrum of the young star HD 100546 observed with the Infrared Space Observatory. *Astron. Astrophys.* **332**, L25–L28 (1998).

21. Grady, C. A. *et al.* Infalling planetesimals in pre-main stellar systems. In *Protostars and Planets IV* (eds Mannings, V., Boss, A. P. & Russell, S. S.) 613–638 (Univ. Arizona Press, 2000).

22. Acke, B. & van den Ancker, M. E. ISO spectroscopy of disks around Herbig Ae/Be stars. *Astron. Astrophys.* (in the press); preprint at ⟨http://xxx.lanl.gov/astro-ph/0406050⟩ (2004).

23. Wetherill, G. W. Formation of the earth. *Annu. Rev. Earth Planet. Sci.* **18**, 205–256 (1990).

24. Dorschner, J., Begemann, B., Henning, T., Jäger, C. & Mutschke, H. Steps toward interstellar silicate mineralogy. *Astron. Astrophys.* **300**, 503–520 (1995).

25. Servoin, J. L. & Piriou, B. Infrared reflectivity and Raman scattering of Mg₂SiO₄ single crystal. *Phys. Status Solidi* **55**, 677–686 (1973).

26. Jäger, C. *et al.* Steps toward interstellar silicate mineralogy. IV. The crystalline revolution. *Astron. Astrophys.* **339**, 904–916 (1998).

27. Spitzer, W. G. & Kleinman, D. A. Infrared lattice bands of quartz. *Phys. Rev.* **121**, 1324–1335 (1961).

28. Min, M., Hovenier, J. W. & de Koter, A. Shape effects in scattering and absorption by randomly oriented particles small compared to the wavelength. *Astron. Astrophys.* **404**, 35–46 (2003).

29. Chihara, H., Koike, C. & Tsuchiyama, A. Low-temperature optical properties of silicate particles in the far-infrared region. *Publ. Astron. Soc. Jpn* **53**, 243–250 (2001).

....

Experimental demonstration of quantum memory for light

Brian Julsgaard[1], **Jacob Sherson**[1,2], **J. Ignacio Cirac**[3], **Jaromír Fiurášek**[4] & **Eugene S. Polzik**[1]

[1]*Niels Bohr Institute, Danish Quantum Optics Center – QUANTOP, Copenhagen University, Blegdamsvej 17, 2100 Copenhagen Ø, Denmark*

[2]*Department of Physics, Danish Quantum Optics Center – QUANTOP, University of Aarhus, 8000 Aarhus C, Denmark*

[3]*Max Planck Institute for Quantum Optics, Hans-Kopfermann-Str. 1, Garching, D-85748, Germany*

[4]*QUIC, Ecole Polytechnique, CP 165, Universite Libre de Bruxelles, 1050 Brussels, Belgium, and Department of Optics, Palacky University, 17. listopadu 50, 77200 Olomouc, Czech Republic*

....

The information carrier of today's communications, a weak pulse of light, is an intrinsically quantum object. As a consequence, complete information about the pulse cannot be perfectly recorded in a classical memory, even in principle. In the field of quantum information, this has led to the long-standing challenge of how to achieve a high-fidelity transfer of an independently prepared quantum state of light onto an atomic quantum state[1–4]. Here we propose and experimentally demonstrate a protocol for such a quantum memory based on atomic ensembles. Recording of an externally provided quantum state of light onto the atomic quantum memory is achieved with 70 per cent fidelity, significantly higher than the limit for classical recording. Quantum storage of light is achieved in three steps: first, interaction of the input pulse and an entangling field with spin-polarized caesium atoms; second, subsequent measurement of the transmitted light; and third, feedback onto the atoms using a radio-frequency magnetic pulse conditioned on the measure-

ment result. The density of recorded states is 33 per cent higher than the best classical recording of light onto atoms, with a quantum memory lifetime of up to 4 milliseconds.

Light is a natural carrier of information in both classical and quantum communications. In classical communications, bits are encoded in large average amplitudes of light pulses, which are detected, converted into electric signals and subsequently stored as charges or magnetization of memory cells. In quantum information processing, information is encoded in quantum states that cannot be accurately recorded by such classical means. Consider a state of light defined by its amplitude and phase, or equivalently by two quadrature phase operators, $\hat{X}_L$ and $\hat{P}_L$, with the canonical commutation relation $[\hat{X}_L,\hat{P}_L] = i$. These variables play the same role in quantum mechanics as the classical quadratures X, P do in the decomposition of the electric field of light with the frequency ω as $E \propto X \cos \omega t + P \sin \omega t$. Other quantum properties of light, such as the photon number $\hat{n} = \frac{1}{2}(\hat{X}_L^2 + \hat{P}_L^2 - 1)$, and so on, can be expressed in terms of $\hat{X}_L$ and $\hat{P}_L$.

The best classical approach to recording a state of light onto atoms would involve homodyne measurements of both observables $\hat{X}_L$ and $\hat{P}_L$ by using, for example, a beam splitter. The non-commutativity of $\hat{X}_L$ and $\hat{P}_L$ leads to additional quantum noise being added during this procedure. The target atomic state has its intrinsic quantum noise (coming from the Heisenberg uncertainty relations). All this extra noise leads to a limited fidelity for the classical recording: for example, to a maximum fidelity of 50% for coherent states[5–7]. Thus the challenge of implementing a quantum memory can be formulated as a faithful storing of the simultaneously immeasurable values of $\hat{X}_L$ and $\hat{P}_L$.

A number of quantum information protocols, such as eavesdropping in quantum cryptography, quantum repeaters[8], and linear optics quantum computing[9], would benefit from a memory meeting the following criteria: (1) the light pulse to be stored is sent by a third party in a state unknown to the memory party; (2) the state of light is converted into a quantum state of the memory with a fidelity higher than that of the classical recording. Several recent experiments[10–13] have demonstrated entanglement of light and atoms. However, none of these experiments demonstrated memory obeying the two above criteria. In ref. 14, where squeezed light was mapped onto atoms, the atomic state existed only while the light was on, so it was not a memory device. The electromagnetically induced transparency (EIT) approach has led to the demonstration of a classical memory for light[15,16]. A theoretical proposal for EIT-based quantum memory for light has been published in ref. 3. Other proposals for quantum memory for light with better-than-classical quality of recording have also been published recently[1–4].

Quantum state transfer from one species to another is most simply presented if both systems are described by canonical quantum variables $\hat{X},\hat{P}$. All canonical variables have the same commutation relations and the same quantum noise for a given state, thus providing a common frame for the analysis of the state transfer.

In the present work, the state of light is stored in the superposition of magnetic sublevels of the ground state of an atomic ensemble. As in ref. 12, we introduce the operator $\hat{J}$ of the collective magnetic moment (orientation) of a ground state F. All atomic states utilized here are not too far in phase space from the coherent spin state (CSS), for which only one projection has a non-zero mean value, for example, $\langle \hat{J}_x \rangle = J_x$, whereas the other two projections have minimal quantum uncertainties, $\langle \delta J_y^2 \rangle = \langle \delta J_z^2 \rangle = \frac{1}{2}J_x$. For all such states, the commutator $[\hat{J}_y,\hat{J}_z] = iJ_x$ can be reduced to the canonical commutator $[\hat{X}_A,\hat{P}_A] = i$ with $\hat{X}_A = \hat{J}_y/\sqrt{J_x}, \hat{P}_A = \hat{J}_z/\sqrt{J_x}$. Hence the y,z-components of the collective atomic angular momentum play the role of canonical variables. Although the memory protocol, in principle, can work with a single atomic ensemble, experimental technical noise is substantially reduced if two oppositely polarized ensembles placed in a bias magnetic field **H** are used (see Methods

and Supplementary Methods for details). Combined canonical variables for two ensembles $\hat{X}_A = (\hat{J}_{y1} - \hat{J}_{y2})/\sqrt{2J_x}$, $\hat{P}_A = (\hat{J}_{z1} + \hat{J}_{z2})/\sqrt{2J_x}$ are then introduced, where $\hat{J}_{x1} = -\hat{J}_{x2} = J_x = FN_{atoms}$. In the presence of **H**, the memory couples to the Ω-sidebands of light: $\hat{X}_L = \frac{1}{\sqrt{T}}\int_0^T (\hat{a}^+(t) + \hat{a}(t))\cos(\Omega t)\mathrm{d}t$, $\hat{P}_L = \frac{i}{\sqrt{T}}\int_0^T (\hat{a}^+(t) - \hat{a}(t))\cos(\Omega t)\mathrm{d}t$, where Ω is the Larmor frequency of spin precession.

Quantum storage of light is achieved in three steps: (1) an interaction of light with atoms; (2) a subsequent measurement of the transmitted light; and (3) feedback onto the atoms conditioned on the measurement result (Fig. 1). The off-resonant interaction of light with spin polarized atomic ensembles has been described elsewhere[4,17–19], and is summarized in the Methods section. The interaction leads to the equations:

$$\hat{X}_L^{out} = \hat{X}_L^{in} + k\hat{P}_A^{in}, \quad \hat{P}_L^{out} = \hat{P}_L^{in}$$
$$\hat{X}_A^{out} = \hat{X}_A^{in} + k\hat{P}_L^{in}, \quad \hat{P}_A^{out} = \hat{P}_A^{in} \qquad (1)$$

These equations imply that light and atoms get entangled. The remarkable simplicity of equations (1) provides a direct link between an input light state, an atomic state, and an output light. Suppose the input light is in a vacuum (or in a coherent) state, and atoms are in a CSS with mean values $\langle \hat{X}_L \rangle = \langle \hat{X}_A \rangle = \langle \hat{P}_L \rangle = \langle \hat{P}_A \rangle = 0$ and variances $\delta X_L^2 = \delta X_A^2 = \delta P_L^2 = \delta P_A^2 = 1/2$. The interaction parameter k, whose value is crucial for the storage protocol, is then readily found as $k^2 = 2(\delta X_L^{out})^2 - 1$.

For a perfect fidelity of mapping, the initial atomic state must be an entangled spin state such as in ref. 12, with $\delta X_A^2 \rightarrow 0$. The pulse to be recorded, combined with the entangling pulse (see Methods section), is sent through, and its variable $\hat{X}_L^{out}$ is measured. The measurement outcome, $x = \hat{X}_L^{in} + k\hat{P}_A^{in}$, is fed back into the atomic variable $\hat{P}_A$ with a feedback gain g. The result is $\hat{P}_A^{mem} = \hat{P}_A^{in} - gx = \hat{P}_A^{in}(1 - kg) - g\hat{X}_L^{in}$ (see Supplementary Notes for a justification of this equation). With $g = k = 1$, the mapping of $\hat{X}_L^{in}$ onto $-\hat{P}_A^{mem}$ is perfect.

The second operator of light is already mapped onto atoms via $\hat{X}_A^{mem} = \hat{X}_A^{in} + \hat{P}_L^{in}$, see equation (1). For the entangled initial state the mapping is perfect for this component too, $\hat{P}_L^{in} \rightarrow \hat{X}_A^{mem}$, leading to the fidelity of the light-to-atoms state transfer $F \rightarrow 100\%$. If the initial atomic state is a CSS, the mapping is not perfect owing to the noisy operator $\hat{X}_A^{in}$. However, fidelity $F = 82\%$, still markedly higher than the classical limit, can be achieved. Note that the above discussion holds for an arbitrary single mode input quantum state of light.

In our experiment, the atomic storage unit consists of two samples of caesium vapour placed in paraffin-coated glass cells placed inside magnetic shields (Fig. 1). **H** is applied along the x-direction with $\Omega = 322\,\mathrm{kHz}$. Optical pumping along **H** initializes the atoms in the first/second sample in the $F = 4$, $m_F = \pm 4$ ground state with the orientation above 99%. Hence $\hat{J}_{x1} = -\hat{J}_{x2} = J_x = 4N_{atoms} \approx 1.2 \times 10^{12}$. We thoroughly check and regularly verify that the initial spin state is close to CSS (Supplementary Methods). The coupling parameter k is varied by adjusting the density of caesium vapour.

The input state $\hat{a}(t)$ is encoded in a 1-ms y-polarized pulse. The state is chosen from the set $\{\hat{a}_{input}\}$ of coherent states with the photon number in the range $\{\langle n \rangle = 0, n_{max}\}$ and an arbitrary phase. $\hat{a}(t)$ is generated as Ω sidebands by an electro-optical modulator (EOM), and has the same spatial and temporal profile as the strong entangling field (more information can be found in the Methods section). Thus the EOM plays the third party, providing the field to be stored. The pulses are detuned by 700 MHz to the blue from the $6S_{1/2}$, $F = 4 \rightarrow 6P_{3/2}$, $F = 5$ transition ($\lambda = 852\,\mathrm{nm}$). The polarization measurement of the light is followed by the feedback onto atoms achieved by a 0.2 ms radio-frequency magnetic pulse conditioned on the measurement result.

The experimental verification of the quantum storage is then carried out. A read-out x-polarized pulse is sent through the samples with a delay of 0.7–10 ms after the feedback is applied. Atomic memory generates a y-polarized pulse, which is analysed as follows. As both $\hat{X}_A^{mem}$ and $\hat{P}_A^{mem}$ cannot be measured at the same time, we carry out two series of measurements for each input state. Each series consists of 10^4 quantum storage sequences. To verify the $\hat{X}_L^{in} \rightarrow -\hat{P}_A^{mem}$ step of the storage, we measure the component $\hat{X}_L^{read-out} = \hat{X}_L^{read-in} + k\hat{P}_A^{mem}$ of the read-out pulse (X_L is a Stokes parameter measured in units of shot noise, as discussed in the Methods section). An example of such a measurement carried out after 0.7 ms of storage is presented in Fig. 2a as a histogram of $\frac{1}{k}\hat{X}_L^{read-out}$ (right histogram), with k measured as described in the Methods section and in Supplementary Methods. For this series $\langle \hat{P}_L^{in} \rangle = -4$ and $\langle \hat{X}_L^{in} \rangle = 0$, corresponding to $\langle \hat{n} \rangle = 8$ photons in the pulse. From this measurement, we find the mean $\langle \hat{P}_A^{mem} \rangle = \frac{1}{k}\langle X_L^{read-out} \rangle$ and the variance $\sigma_P^2 = \langle (\delta \hat{P}_A^{mem})^2 \rangle = \frac{1}{k^2}((\delta X_L^{read-out})^2 - \frac{1}{2})$ (see equations (1)) for the quantum state of the memory. We note that only the knowledge of k and the shot noise level of light is necessary for the determination of the mean values and variances of the atomic canonical variables from the experimental data.
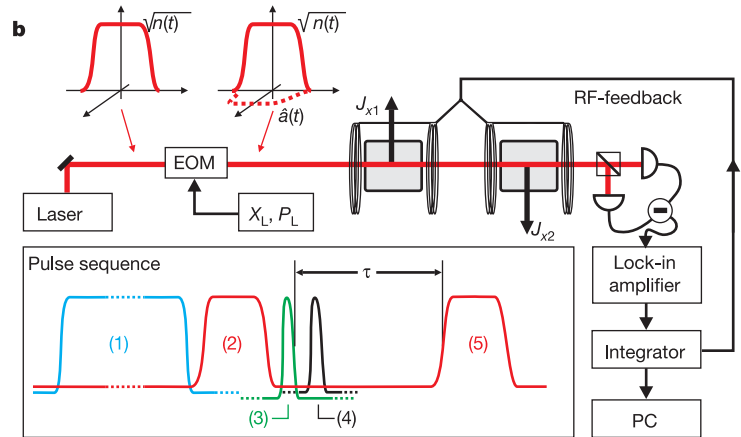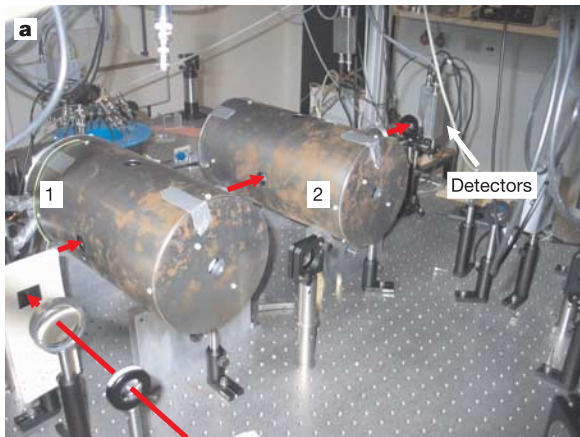

Figure 1 Experimental set-up. **a**, Atomic memory unit consisting of two caesium cells inside magnetic shields 1 and 2. The path of the recorded and read-out light pulses is shown with arrows. **b**, The simplified layout of the experiment. The input state of light with the desired displacements X_L, P_L is generated with the electro-optic modulator (EOM). The inset shows the pulse sequence for the quantum memory recording and read-out.

Pulse (1) is the optical pumping (4 ms), pulse (2) is the input light pulse $\hat{a}(t)$ overlapped with the strong entangling pulse in orthogonal polarization with amplitude $\sqrt{n(t)}$. Pulse (3) is the magnetic feedback pulse. Pulse (4) is the magnetic $\pi/2$ pulse used for the read out of one of the atomic operators. Pulse (5) is the read-out optical pulse.

Next, we run another series of storage with the same input state for the verification of the step $\hat{P}_L^{in} \rightarrow \hat{X}_A^{mem}$. The $\hat{X}_A^{mem}$ operator does not couple to the read-out pulse in our geometry; therefore, we first apply a $\pi/2$-pulse (Fig. 1) to atoms converting $\hat{X}_A^{mem} \rightarrow \hat{P}_A^{\pi}$ and then measure $\hat{P}_A^{\pi}$ with the verifying pulse. We then find $\langle \hat{X}_A^{mem} \rangle$ and $\sigma_x^2 = \langle (\delta \hat{X}_A^{mem})^2 \rangle$ of the memory state (left histogram).

The above sequence is repeated for different input states. From $\langle \hat{P}_A^{mem} \rangle / \langle \hat{X}_L^{in} \rangle$ and $\langle \hat{X}_A^{mem} \rangle / \langle \hat{P}_L^{in} \rangle$, the mapping gains for the two quadratures are determined. For the experimental data presented in Figs 2 and 3a, these gains are 0.80 and 0.84 respectively, which is close to the optimal gain for the chosen input set of states. This step would complete the proof of the classical memory performance, because we have shown that the y-polarized pulse recovered from the memory has the same mean amplitude and mean phase as the input pulse (up to a chosen constant factor).

To prove a quantum memory performance, we need in addition to consider the quantum noise of the stored state. Towards this end, we plot the atomic variances σ_p^2, σ_x^2 for the storage time 0.7 ms in Fig. 3a. The experimentally obtained variances of the stored state are on average 33% below the best possible variance of the classical recording. Hence a density of stored states 33% higher than that for the best classical recording can be obtained. Thus the goal of

quantum storage with less noise than for the classical recording is achieved.

Next, the overlap between the input state of light and the state of the atomic memory is determined (Methods section). An example is shown in Fig. 2b. The fidelity F of the quantum recording is then calculated for a given set $\{\hat{a}_{input}\}$. For example, $F = (66.7 \pm 1.7)\%$ for $\{\hat{a}_{input}\} = \{n = 0 \rightarrow 8\}$ and $F = (70.0 \pm 2.0)\%$ for $\{\hat{a}_{input}\} = \{n = 0 \rightarrow 4\}$, respectively, for the storage time of 0.7 ms. Note that the fidelity of the classical recording can exceed 50% for a limited set $\{\hat{a}_{input}\}$. The maximum classical fidelity for $\{\hat{a}_{input}\} = \{n = 0 \rightarrow 8\}$ is 55.4%, and for $\{\hat{a}_{input}\} = \{n = 0 \rightarrow 4\}$ it is 59.6%—still significantly lower than that for the quantum recording.

The main sources of imperfection of our quantum memory are decoherence of the atomic state and reflection off the cell walls. We have performed extensive studies of the atomic decoherence caused by the light-assisted collisional relaxation[20] to optimize the fidelity. Figure 3b presents the fidelity of the stored state as a function of the storage time. A simple model provides a good description for the observed fidelity reduction.

The single observable read-out described above can be useful in, for example, quantum cryptography eavesdropping, where the memory is read after the basis has been publicly announced by
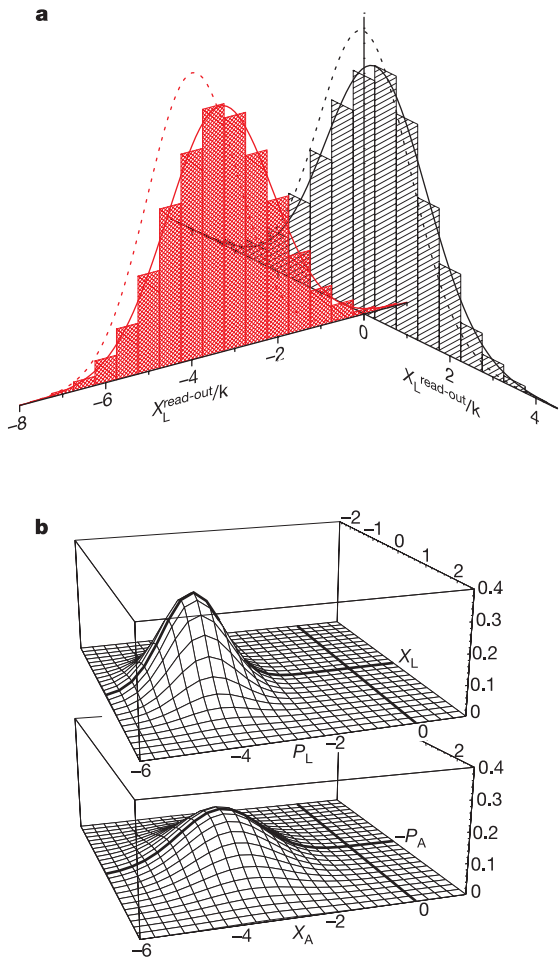

Figure 2 An example of the atomic memory performance. **a**, The input state of light in the coherent state with $\langle \hat{X}_L \rangle = 0, \langle \hat{P}_L \rangle = -4$. The results of the read out of this state stored in the atomic memory are shown as histograms of experimental realizations. The left/right histogram shows the results for the $\hat{X}_A/\hat{P}_A$ quadrature read out with/without the $\pi/2$-pulse. Dotted gaussians represent the distributions for the best possible quantum memory performance (fidelity 100%). **b**, The input coherent state of light (upper graph) and the reconstructed state stored in the atomic memory (lower graph) for the input state as in **a**. The reconstructed state is obtained from the results presented in **a** after subtracting the noise of the read-out pulse.
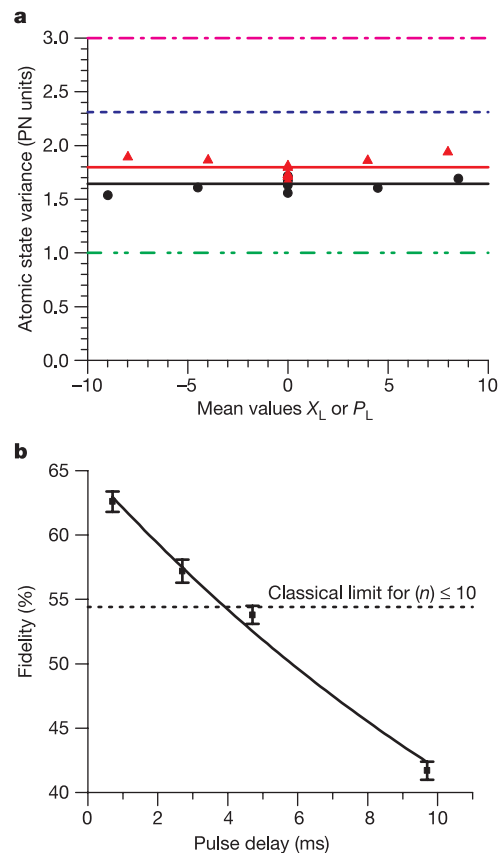

Figure 3 Quantum noise of the stored state and the fidelity of quantum memory as a function of time. **a**, Experimental and theoretical (quantum and classical) stored state variances in atomic projection noise (PN) units. Triangles and filled circles are the experimental variances for the atomic memory operators, denoted $2\sigma_x^2$ and $2\sigma_p^2$, respectively, in the text. Dash-dotted line, the fundamental boundary of three units of noise between quantum and classical mapping for an arbitrary coherent input state[5,6]. Dashed line, best classical variance for the experimental set of input states with photon numbers between 0 and 8. Double-dot-dashed line, unity variance corresponding to perfect mapping. **b**, Fidelity as a function of storage time for the set of states from 0 to 10 photons. Fidelity higher than the classical limit is maintained for up to 4 ms of storage. Error bars are standard deviations.

Alice and Bob. The present experiment also paves the way towards the proposed quantum cloning of light onto atomic memory[21]. However, other applications require complete state recovery via reverse mapping of the memory state onto light. Proposals for performing this task within our approach have been published[4,19,22]. Probably the most intuitively clear protocol for the memory read-out is just to run the storage protocol presented here with reversed roles of light and atoms. Indeed, the equations of interaction (1) are completely symmetric. The read-out, as the storage, would involve three steps: sending a read-out light pulse through atoms, measuring the spin projection $\hat{X}_A^{out}$ with an auxiliary light pulse, and applying the feedback conditioned on this measurement to the read-out pulse.

In the present experiment, we have demonstrated the memory for a subset of linearly independent coherent states. Owing to the linearity of quantum mechanics, this demonstration signifies that our method provides faithful mapping for an arbitrary coherent state. As any arbitrary quantum state can be written as a super-position of coherent states, our approach should in principle work for an arbitrary quantum state, including entangled and single photon (qubit) states. □

Methods

Quantum coupling of light to two atomic ensembles in the presence of magnetic field

Here we discuss the physics behind the equations of interaction (1). The off-resonant atom/light interaction is described in terms of Stokes operators for the polarization state of light and the collective spin of atoms[4,17,18]. The Stokes operators are defined as one half of the photon number difference between orthogonal polarization modes: $\hat{S}_1$, between vertical x- and horizontal y-polarizations; $\hat{S}_2$, between the modes polarized at $\pm 45°$ to the vertical axis; and $\hat{S}_3$, between the left- and right-hand circular polarizations. In the experiment, a strong entangling x-polarized pulse with photon flux $n(t)$ is mixed on a polarizing beamsplitter with the y-polarized quantum field $\hat{a}(t)$ prior to interaction with atoms. Hence the Stokes operators of the total optical field are $\hat{S}_1(t) = S_1(t) = \frac{1}{2}n(t)$, $\hat{S}_2 = \frac{1}{2}\sqrt{n(t)}(\hat{a}^+(t) + \hat{a}(t))$, $\hat{S}_3 = \frac{i}{2}\sqrt{n(t)}(\hat{a}^+(t) - \hat{a}(t))$. Note that $\hat{S}_2(t)$ and $\hat{S}_3(t)$ are proportional to the canonical variables for the quantum light mode, $\hat{X} = \frac{1}{\sqrt{2}}(\hat{a}^+(t) + \hat{a}(t))$, $\hat{P} = \frac{i}{\sqrt{2}}(\hat{a}^+(t) - \hat{a}(t))$. Light is transmitted through the atomic samples placed in the bias magnetic field oriented along the x-axis. The magnetic field allows for encoding of the memory at the Larmor frequency Ω, thus dramatically reducing technical noise present at low frequencies. However, in the presence of the Larmor precession, there is an undesired coupling of the single-cell variables $\hat{J}_y$ and $\hat{J}_z$ to each other. The introduction of the second cell with the opposite Larmor precession allows us to introduce new two-cell variables $(\hat{J}_{y1} - \hat{J}_{y2})$, $(\hat{J}_{z1} + \hat{J}_{z2})$ that do not couple to each other. As in ref. 12, where a similar trick was used, the Stokes parameters of light transmitted through the two cells along the z direction become:

$$\hat{S}_2^{out}(t) = \hat{S}_2^{in}(t) + aS_1(\cos(\Omega t)[\hat{J}_{z1} + \hat{J}_{z2}] + \sin(\Omega t)[\hat{J}_{y1} + \hat{J}_{y2}]), \quad \hat{S}_3^{out}(t) = \hat{S}_3^{in}(t) \quad (2)$$

where $\hat{J}_{z,y}$ are the projections in the frame rotating at Ω, and $a = \frac{\gamma \lambda^2}{8\pi A\Delta}$, with γ and λ the natural linewidth and the wavelength of the transition, respectively, Δ the detuning, and A the beam cross-section. At the same time, the transverse spin components of the two cells evolve as follows:

$$\frac{d}{dt}[\hat{J}_{z1} + \hat{J}_{z2}] = \frac{d}{dt}[\hat{J}_{y1} + \hat{J}_{y2}] = 0,$$

$$\frac{d}{dt}[\hat{J}_{y1} - \hat{J}_{y2}] = 2aJ_x\hat{S}_3^{in}\cos(\Omega t), \quad \frac{d}{dt}[\hat{J}_{z1} - \hat{J}_{z2}] = 2aJ_x\hat{S}_3^{in}\sin(\Omega t) \quad (3)$$

As evident from equation (3), in the process of propagation the operator $\hat{S}_3^{in}$ is recorded onto the operators $\hat{J}_{y1} - \hat{J}_{y2}$ and $\hat{J}_{z1} - \hat{J}_{z2}$ (the 'back action' of light on atoms via the dynamic Stark effect caused by light[17,18]), while the operators $\hat{J}_{y1} + \hat{J}_{y2}$ and $\hat{J}_{z1} + \hat{J}_{z2}$ are left unchanged. The latter are read out onto $\hat{S}_2^{out}$ via the Faraday rotation, equation (2).

Canonical variables are defined for the quantum light mode as $\hat{X}_L = \frac{1}{\sqrt{T}}\int_0^T(\hat{a}^+(t) + \hat{a}(t))\cos(\Omega t)dt$, $\hat{P}_L = \frac{i}{\sqrt{T}}\int_0^T(\hat{a}^+(t) - \hat{a}(t))\cos(\Omega t)dt$; that is, the relevant light mode involves the Ω-sidebands. T is the pulse duration, $\hat{a}(t)$ is normalized to the photon flux. $\hat{X}_L$ and $\hat{P}_L$ (that is, $\hat{S}_2$ and $\hat{S}_3$) are detected by a polarization state analyser and by lock-in detection of the Ω component of the photocurrent. Note that the $\cos(\Omega t)$ component of light couples to the $(\hat{J}_{y1} - \hat{J}_{y2})$, $(\hat{J}_{z1} + \hat{J}_{z2})$ components of atomic spin variables (equations (2), (3)). The equivalent choice of a $\sin(\Omega t)$ modulation instead would mean the use of $(\hat{J}_{y1} + \hat{J}_{y2})$, $(\hat{J}_{z1} - \hat{J}_{z2})$ for the memory. The atomic canonical variables $\hat{X}_A$, $\hat{P}_A$ are defined in the main section. With the above equations and definitions we straightforwardly derive equations (1) under the assumption $\Omega T \gg 1$. Theoretically, the dimensionless coupling parameter in (1) is $k^2 = \frac{1}{2}a^2 J_x \int n(t)dt$.

Experimental calibration of the canonical variances for light and atoms

Calculations of the fidelity, the gains, and the variances from the experimental data are based on the experimental calibration of $\langle \delta \hat{X}_L^2 \rangle = \langle \delta \hat{P}_L^2 \rangle$ for the coherent (vacuum) state of light and of $\langle \delta \hat{X}_A^2 \rangle = \langle \delta \hat{P}_A^2 \rangle$ for the CSS of atoms. The calibration for light is carried out along the established procedure of determining the shot noise level for measurements of

$\hat{S}_2$, $\hat{S}_3$ with the quantum field in a vacuum state[5,17]. Variances and mean values for light are then measured in units of this shot noise level. The calibration for the atomic CSS variance is carried out with extreme care, and has shown excellent reproducibility (see Supplementary Methods). As stated in the main text, as soon as the vacuum (shot) noise level for light is established and the atoms are in a CSS, the parameter k^2 (equations (1)), important for calculations of atomic variances and fidelity, is easily determined as $k^2 = 2(\delta X_L^{out})^2 - 1$. In the experiment, this is equivalent to $k^2 = \left((\delta S_2^{out})^2 - (\delta S_2^{in})^2\right)/(\delta S_2^{in})^2$.

Fidelity and the state overlap

To calculate the fidelity of the transfer of an input coherent state into an output gaussian state[6], we first define an overlap function between an input state with mean values x_1, p_1 and the output state with the mean values and variances x_2, p_2, σ_x^2, σ_p^2. Straightforward integration yields:

$$O\{x_1, x_2, p_1, p_2\} = 2\exp(-(x_1 - x_2)^2/(1 + 2\sigma_x^2)$$

$$- (p_1 - p_2)^2/(1 + 2\sigma_p^2))/\sqrt{\left(1 + 2\sigma_x^2\right)\left(1 + 2\sigma_p^2\right)}$$

The fidelity of the transfer for a set of coherent states with mean amplitudes between α_1 and α_2 can then be found as an average overlap:

$$F = \pi^{-1}\left(\alpha_2^2 - \alpha_1^2\right)^{-1}\int_0^{2\pi}d\phi\int_{\alpha_1}^{\alpha_2}O\{\alpha\}\alpha d\alpha$$

For classical recording from light onto atoms with gain g, the overlap between the input coherent state with the mean amplitude $\alpha = \sqrt{x^2 + p^2}$ and the output state is given by $O\{\alpha\} = (1 + g^2)^{-1}\exp\left(-\frac{1}{2}(1 - g)^2\alpha^2(1 + g^2)^{-1}\right)$. The classical fidelity is then given by:

$$F_{class} = (n_2 - n_1)^{-1}(1 - g)^{-2}\{\exp(-(1 - g)^2 n_1(1 + g^2)^{-1})$$

$$- \exp(-(1 - g)^2 n_2(1 + g^2)^{-1})\}$$

where we have introduced the mean photon number $n = \frac{1}{2}\alpha^2$. $F_{class} \rightarrow 50\%$ for arbitrary coherent states when $g \rightarrow 1$. If a restricted class of coherent states is chosen as the input, $F_{class} > 50\%$ can be obtained with a suitable choice of g. For a set of states analysed in the main text, $\{\hat{a}_{input}\} = \{n = 0 \rightarrow 8\}$, the maximum classical fidelity of 55.4% is achieved with a gain of 0.809.

1. Cirac, J. I., Zoller, P., Kimble, H. J. & Mabuchi, H. Quantum state transfer and entanglement distribution among distant nodes in a quantum network. *Phys. Rev. Lett.* **78**, 3221–3224 (1997).
2. Kozhekin, A. E., Mølmer, K. & Polzik, E. S. Quantum memory for light. *Phys. Rev. A* **62**, 033809 (2000).
3. Fleischhauer, M. & Lukin, M. D. Quantum memory for photons: dark-state polaritons. *Phys. Rev. A* **65**, 022314 (2002).
4. Kuzmich, A. & Polzik, E. S. in *Quantum Information with Continuous Variables* (eds Braunstein, S. L. & Pati, A. K.) 231–265 (Kluwer, Dordrecht, 2003).
5. Furusawa, A. *et al.* Unconditional quantum teleportation. *Science* **282**, 706–709 (1998).
6. Van Loock, P., Braunstein, S. L. & Kimble, H. J. Broadband teleportation. *Phys. Rev. A* **62**, 022309 (2000).
7. Hammerer, K., Wolf, M. M., Polzik, E. S. & Cirac, J. I. Quantum benchmark for storage and transmission of coherent states. Preprint at ⟨http://xxx.lanl.gov/quant-ph/0409109⟩ (2004).
8. Briegel, H. J., Dur, W., Cirac, J. I. & Zoller, P. Quantum repeaters: The role of imperfect local operations in quantum communication. *Phys. Rev. Lett.* **81**, 5932–5935 (1998).
9. Knill, E., Laflamme, R. & Milburn, G. J. A scheme for efficient quantum computation with linear optics. *Nature* **409**, 46–53 (2001).
10. van der Wal, C. H. *et al.* Atomic memory for correlated photon states. *Science* **301**, 196–200 (2003).
11. Kuzmich, A. *et al.* Generation of nonclassical photon pairs for scalable quantum communication with atomic ensembles. *Nature* **423**, 731–734 (2003).
12. Julsgaard, B., Kozhekin, A. & Polzik, E. S. Experimental long-lived entanglement of two macroscopic objects. *Nature* **413**, 400–403 (2001).
13. Blinov, B. B., Moehring, D. L., Duan, L. M. & Monroe, C. Observation of entanglement between a single trapped atom and a single photon. *Nature* **428**, 153–157 (2004).
14. Hald, J., Sørensen, J. L., Schori, C. & Polzik, E. S. Spin squeezed atoms: A macroscopic entangled ensemble created by light. *Phys. Rev. Lett.* **83**, 1319–1322 (1999).
15. Liu, C., Dutton, Z., Behroozi, C. H. & Hau, L. V. Observation of coherent optical information storage in an atomic medium using halted light pulses. *Nature* **409**, 490–493 (2001).
16. Phillips, D. F., Fleischhauer, A., Mair, A., Walsworth, R. L. & Lukin, M. D. Storage of light in atomic vapor. *Phys. Rev. Lett.* **86**, 783–786 (2001).
17. Schori, C., Julsgaard, B., Sørensen, J. L. & Polzik, E. S. Recording quantum properties of light in a long-lived atomic spin state: Towards quantum memory. *Phys. Rev. Lett.* **89**, 057903 (2002).
18. Julsgaard, B., Schori, C., Sørensen, J. L. & Polzik, E. S. Atomic spins as a storage medium for quantum fluctuations of light. *Quant. Inform. Comput.* **3** (special issue), 518–534 (2003).
19. Kuzmich, A. & Polzik, E. S. Atomic quantum state teleportation and swapping. *Phys. Rev. Lett.* **85**, 5639–5642 (2000).
20. Julsgaaard, B., Sherson, J., Sørensen, J. L. & Polzik, E. S. Characterizing the spin state of an atomic ensemble using the magneto-optical resonance method. *J. Opt. B* **6**, 5–14 (2004).
21. Fiurášek, J., Cerf, N. J. & Polzik, E. S. Quantum cloning at the light-atoms interface: copying a coherent light state into two atomic quantum memories. *Phys. Rev. Lett.* (in the press); preprint at ⟨http://xxx.lanl.gov/abs/quant-ph/0404054⟩ (2004).
22. Hammerer, K., Mølmer, K., Polzik, E. S. & Cirac, J. I. Light-matter quantum interface. *Phys. Rev. A* (in the press); preprint at ⟨http://xxx.lanl.gov/abs/quant-ph/0312156⟩ (2004).

letters to nature

Correspondence and requests for materials should be addressed to E. P. (polzik@nbi.dk).

....

Direct observation of the discrete character of intrinsic localized modes in an antiferromagnet

M. Sato & A. J. Sievers

Laboratory of Atomic and Solid State Physics and Cornell Center for Materials Research, Cornell University, Ithaca, New York 14850-2501, USA

....

In a strongly nonlinear discrete system, the spatial size of an excitation can become comparable to, and influenced by, the lattice spacing. Such intrinsic localized modes (ILMs)—also called 'discrete breathers' or 'lattice solitons'—are responsible for energy localization in the dynamics of discrete nonlinear lattices[1–5]. Their energy profiles resemble those of localized modes of defects in a harmonic lattice but, like solitons, they can move (although, unlike solitons, some energy is exchanged during collisions between them). The manipulation of these localized energy 'hotspots' has been achieved in systems as diverse as annular arrays of coupled Josephson junctions[6,7], optical waveguide arrays[8], two-dimensional nonlinear photonic crystals[9] and micromechanical cantilever arrays[10]. There is also some evidence for the existence of localized excitations in atomic lattices[11–15], although individual ILMs have yet to be identified. Here we report the observation of countable localized excitations in an antiferromagnetic spin lattice by means of a nonlinear spectroscopic technique. This detection capability permits the properties of individual ILMs to be probed; the disappearance of each ILM registers as a step in the time-dependent signal, with the surprising result that the energy staircase of ILM excitations is uniquely defined.

Rod-shaped samples of the quasi-one-dimensional antiferromagnet, $(C_2H_5NH_3)_2CuCl_4$, are used in this study[13,16–18] so that the antiferromagnetic resonance (AFMR) frequency occurs at the bottom of the spin-wave manifold. Mesoscale, high spin-precession amplitude, magnetic ILMs can then be produced in the gap below this band because of the soft nonlinearity of the spin lattice. As outlined in Fig. 1a, there are four fundamental sequential time steps required for these energy localization experiments: (1) a uniform spin wave mode of the biaxial antiferromagnet is driven to a large precession amplitude by an initial microwave pulse (frequency f_1); (2) after an incubation period, the modulational instability of the large amplitude uniform mode takes hold, producing many ILMs in a broad frequency band[19]; (3) a few of these ILMs are then locked[20,21] to the continuous wave (c.w.) middle power source f_2; and, finally, (4) the experiment of interest, where a c.w. low power source f_3 is used to produce a mixing signal that depends on the number of ILMs in the lattice. After a spin-lattice relaxation time of $T_1 = 1.5$ ms, the number of ILMs is determined by a quasi-steady state involving the f_2 driver and the nonequilibrium AFMR[13], and this number is expected to decrease as this frequency difference increases.
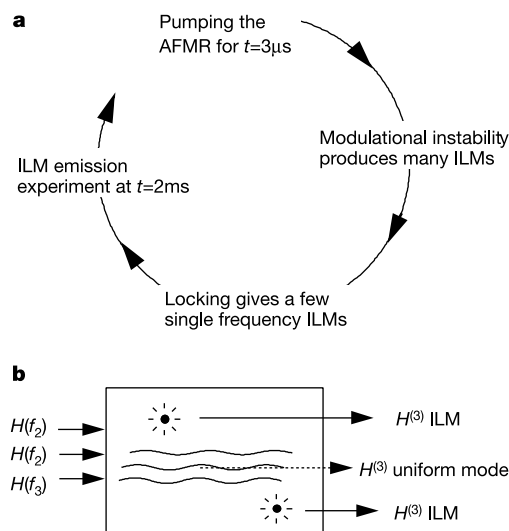

Figure 1 Schematic diagrams of the experimental procedure and the nonlinear process. **a**, The chronological timing in the nonlinear energy magnetometer is shown for the production and measurement of intrinsic localized modes (ILMs). AFMR, antiferromagnetic resonance. **b**, Nonlinear mixing output for uniform excitations and for ILMs. Large filled circles represent ILMs. Although small in number because of locking, these strong nanoscale third order mixing elements dominate the output signal. Two inputs are from the locking driver field $H(f_2)$ and the remainder is from the probe field $H(f_3)$, giving a maximum output at $2f_2 - f_3$. Each ILM generates a nonlinear field $H^{(3)}$. As the mixed signal power depends on the square of the total field, the square root of the power is proportional to the number of ILMs.

Because the number of spins in an ILM is too small to be seen in absorption, a nonlinear energy magnetometer has been developed, which automatically handles the four time steps for this low temperature ILM production and detection experiment. It relies on the third-order nonlinearity $\chi^{(3)}$ of the antiferromagnet[22–24] to make observable in nonlinear emission the small number of ILMs that remain locked to the f_2 driver, as illustrated in Fig. 1b. Nonlinear and linear excitations in the same sample give very different nonlinear responses: the signal produced by ILMs is enhanced, while that produced by the small precession amplitude extended plane wave states, which are nearly harmonic, is suppressed. This nonlinear discrimination feature of the instrument brings the few nanoscale ILMs out of the background of plane wave states for experimental exploration.

Presented in Fig. 2a is the power spectrum produced at f_3, where $2f_2 - f_3 = f_{det}$, and both f_3 and f_{det}, the narrow band detector frequency, are scanned in tandem. Typical frequency positions for f_1, f_2 and the near-equilibrium AFMR are identified at the top of Fig. 2. The strong emission peak from the locked ILMs (see arrow) is observed shifted to slightly lower frequencies from the f_2 locking oscillator (about 4 MHz), while a somewhat weaker peak is shifted up in frequency. (These sidebands represent a form of cross phase modulation for the ILMs.) The logarithmic plot shown in Fig. 2b displays more clearly the other weaker spectral features, as well as the excellent signal to noise level for these measurements. The weak peak observed at 1.362 GHz (see top right arrow) occurs when f_3 matches the AFMR frequency in a resonant four wave mixing process at $T \approx 2$ ms. This weak feature at long times is independent of whether or not the f_1 pulse is applied and, hence, is a property of the homogeneous solid. When ILMs are produced, they encompass states originally associated with the spin wave band; however, because of the small number of ILMs studied (that is, only a few ILMs remain locked), 99.999% of the spins are in the low amplitude homogeneous state. Figure 2b demonstrates that although the AFMR involves many spins, off resonance it is a very weak nonlinear mixer.